

# We are IntechOpen, the world's leading publisher of Open Access books Built by scientists, for scientists

6,900

Open access books available

186,000

International authors and editors

200M

Downloads

Our authors are among the

154

Countries delivered to

TOP 1%

most cited scientists

12.2%

Contributors from top 500 universities



WEB OF SCIENCE™

Selection of our books indexed in the Book Citation Index  
in Web of Science™ Core Collection (BKCI)

Interested in publishing with us?  
Contact [book.department@intechopen.com](mailto:book.department@intechopen.com)

Numbers displayed above are based on latest data collected.  
For more information visit [www.intechopen.com](http://www.intechopen.com)



---

# Turbulence Transport in Rotor-Stator and Stator-Rotor Stages of Axial Flow Fans

---

Jesús Manuel Fernández Oro,  
Andrés Meana Fernández and Bruno Pereiras García

Additional information is available at the end of the chapter

<http://dx.doi.org/10.5772/67751>

---

## Abstract

Turbulence analysis in turbomachines is a complex task. The combination of different turbulence sources and transport mechanisms poses the question of determining adequate metrics to quantify turbulence levels and provide insight into the flow structure and its evolution. Apart from experimental measurement techniques, numerical techniques arise as a useful tool to characterize this type of flow, especially hybrid LES techniques that allow a highly accurate description of the transport of turbulent structures, while turbulence generation at solid boundaries is addressed using RANS schemes. In this chapter, recent developments concerning numerical simulation of rotor-stator and stator-rotor interactions in low-speed axial fans using LES techniques are presented. A post-processing framework is introduced to segregate the deterministic and turbulent components of the unsteady flow, allowing an accurate description of both phenomena. Hence, turbulent transport over the different stage rows of the axial fan can be accurately addressed. Following, LES capacities to simulate turbulence transport mechanisms such as breaking-up of turbulent eddies, stretching and dissipation of vorticity or identification and convection of coherent vortices are discussed. The ability of LES computations to disclose flow turbulence in rotor-stator environments at off-design conditions is specially illustrated.

**Keywords:** turbulence metrics, turbulence transport, LES simulations, rotor-stator interaction

---

## 1. Introduction

Turbulence analysis in single-stage turbomachines, like axial fans, is a complex task. Firstly, there is turbulence generation in both fixed (stator) and moving (rotor) reference frames.

---

Then, these turbulent scales and patterns are transported across the frames, interacting between them and developing secondary turbulent sources. Furthermore, unless the stages are designed under free-vortex criteria, there is a further swirl of the motion that leads to radial migration of momentum and turbulence. Finally, there are additional types of interactions that contribute to generate further turbulence, like the interaction between wakes, the interaction between wakes and blades or vanes, or even interactions between wakes, tip vortices and endwalls.

This combination of different turbulence sources and transport mechanisms poses the question of determining adequate metrics to quantify turbulence levels and give insight into the flow structure and its evolution within this kind of machines.

Apart from experimental measurement techniques such as hot-wire anemometry (HWA) or particle-image velocimetry (PIV), able to capture the turbulent variations of the flow inside these axial fans, numerical techniques arise as a useful tool to characterize this type of flows. Nowadays, scale-resolving simulations (SRS) [1] are becoming the standard to simulate the turbulent flow in multistage environments, being large eddy simulations (LES) the cornerstone of the methodology. On the contrary, U-RANS modelling is being progressively abandoned due to the continuous improvements of the computing capabilities [2].

However, fully-LES techniques are still excessively time-consuming and, in most cases, unaffordable because of the extremely refined meshes required for the boundary layers of the solid walls.

In this context, wall-modelled LES (WMLES) [3] and embedded LES (ELES) are hybrid techniques that allow a highly accurate description of the transport of the turbulent structures, while the generation in solid boundaries is still addressed using RANS schemes. LES computations in the vicinity of the turbomachinery rows are able to capture the turbulent variations up to the frequency related to the LES filter, which depends on the grid size. With an accurate selection of this size, it is possible to capture most of the turbulent kinetic energy of the larger and mid-scale vortices, which content practically all the significant portion of turbulent motion.

In this chapter, recent developments concerning numerical simulation of rotor-stator (R-S) and stator-rotor (S-R) interactions in low-speed axial fans using LES techniques are presented. In particular, LES capacities to simulate transport mechanisms for turbulence such as breaking-up of turbulent eddies, stretching and dissipation of vorticity or identification and convection of coherent vortices are discussed. The ability of LES computations to deal with the flow turbulence in rotor-stator environments at off-design conditions is specially illustrated.

## **2. Turbulent scales and periodic unsteadiness in rotating fans**

Turbulence generation associated to vortex shedding in rotor blades is perceived as a periodic impingement of turbulent wakes on stator flow structures in R-S stages. Alternatively, the rotor flow structures are also affected by the incoming non-uniformities from the upstream

vanes in S-R arrangements. Thus, turbulent structures are superimposed to the velocity deficit associated to the rotor blockage, travelling unsteadily across the fan stage [4]. Due to the high Reynolds numbers, turbulence in the shear layers is rolled-up at quite small scales, significantly smaller than typical displacement thicknesses of the wake deficit.

**Figure 1** shows a typical representation of the amplitude of the LES-resolved velocity fluctuations in the vicinity of the rotor for a single stage axial fan. Typical scales (frequency ranges) corresponding to forced and unforced unsteadiness, as well as turbulence, have been indicated in **Figure 1** for nominal and offset working conditions. Turbulence is clearly associated to the smallest length scales (higher frequencies). The energy budget of turbulent phenomena, including free-stream, generation at endwall boundary layers and wake-induced turbulence, presents a classic broadband distribution. As expected, turbulent scales are more evident at off-design conditions (grey lines). Forced unsteadiness is perfectly identifiable at blade passing frequencies (BPF) and its harmonics (sharp peaks), while unforced contributors are related to other periodic features non-locked with the BPF, like blade misalignments, tip vortex instabilities or unsteadiness in separation conditions [5]. This kind of unsteadiness is strictly associated to a particular time scale, so it contains very important flow patterns, but

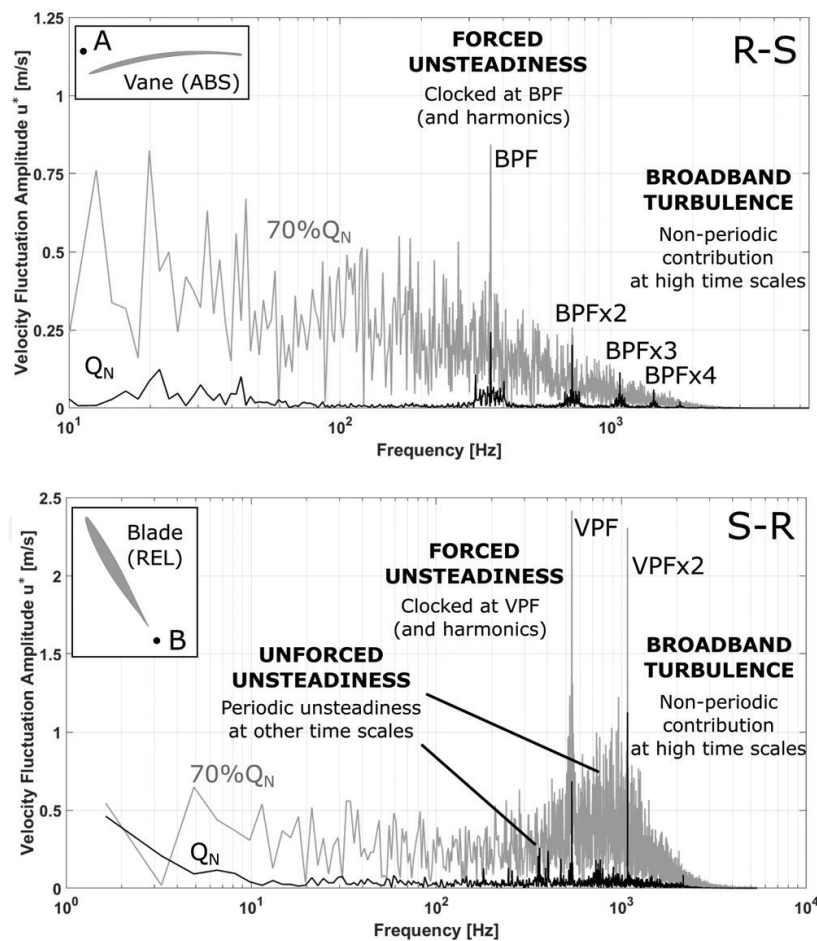


**Figure 1.** Typical scales of unsteadiness and turbulence for a single stage axial fan at different flow rates (top: R-S configuration, bottom: S-R configuration).

with a moderate energy budget. Note the particularity of the S-R configuration values, which are computed in the relative frame of reference, so the frequency peaks appear at an apparent 'vane-passing frequency' and its harmonics. Additionally, due to the flow complexity, interaction between the broadband turbulence and peaked frequencies (clocked at BPF/VPF or not) may arise, which obscures the analysis of the different contributions to the total unsteadiness (see the S-R configuration for the 70%  $Q_N$  case, which clearly presents a turbulent hump between VPF and  $VPF \times 2$ ).

Consequently, to obtain a proper analysis of the turbulent characteristics, it is convenient to segregate between turbulent scales and unsteady events with special care. Otherwise, only a total unsteadiness is found in the analysis, including turbulent fluctuations as well as the non-stationary effects due to the periodical rotation of the machine blades. This procedure results in a superficial analysis of turbulence, especially for the turbulent transport.

The correct procedure requires that the instantaneous values of the measured variable are grouped in ensembles corresponding to the blade-passing frequency [6]. Then, mean values for every blade position are calculated, obtaining a signal that contains only the unsteadiness due to the rotation of the machine (periodical or deterministic unsteadiness). These ensemble-averaging values, combined with the time-averaging value of the complete signal, enable the segregation of the total unsteadiness of the measured variable into its deterministic and turbulent parts.

This segregation can be performed in both time and frequency domains [7]. Though strictly, performing ensemble averages at BPF in the time domain should be sufficient, the complex nature of the vortical motion and the interchange of energy in the viscous cascade within a sea of all-range eddies makes an exact segregation impossible. Sometimes, the use of a frequency decomposition is also required in order to decouple forced and unforced unsteadiness from turbulence [8].

### 3. Numerical methods: LES simulations in R-S and S-R configurations

A typical low-speed, single-stage axial fan will be considered for the computations. Because of its free-vortex rotor design, it will be assumed that the flow is quasi-planar in the mid-span sections, working in a cascade mode (**Figure 2**, left). The mesh density within the passages has been carefully selected in order to describe vortical structures in the range of the integral length scales when large separation arises (i.e. rotor wakes shedding at 70%  $Q_N$ ). For both blades and vanes surfaces, a typical O-grid distribution with a  $[100 \times 60]$  mesh density was considered sufficient to model the boundary layers. Additionally, the  $z$ -coordinate for the spanwise direction was covered with 15 cells, for a total height of the model of 0.12 blade chords, following the guidelines proposed by Davidson and Dahlström [9]. As a result, a total number of 3.4 and 3.6M cells were resolved for the R-S and S-R domains, respectively.

The sliding mesh technique has been employed in the computations with FLUENT® to simulate the relative movement of the rotor blades with respect to the stator vanes. In the present case, a time step of  $9.26 \times 10^{-5}$  s has been fixed, which implies 30 intermediate time steps per

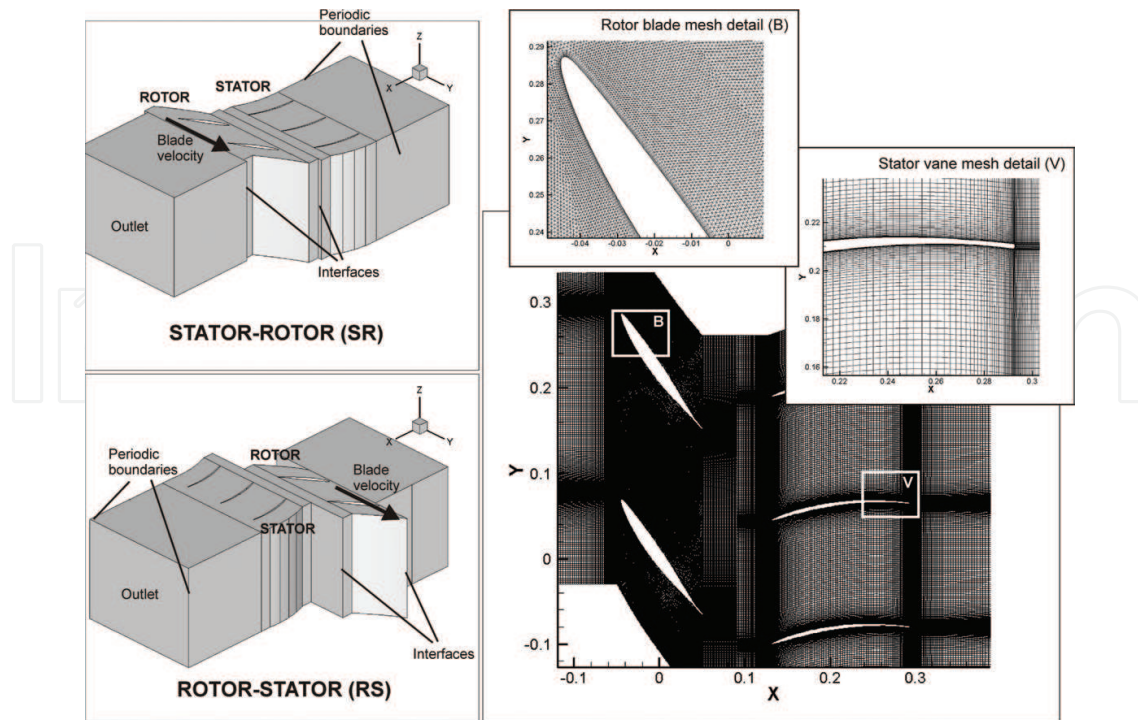


**Figure 2.** Stator-rotor and rotor-stator in linear cascade (left). Mesh densities in stator and rotor rows: details in the trailing edge of the vanes and leading edge of the blades (right).

blade event, being able to resolve the turn-out time of the resolved eddies in the LES scheme. All these assumptions, based on the extrusion of a two-dimension (2D) section of the fan with periodic conditions, have been already experimentally verified [10] for three different operating conditions: 100, 85 and 70% of the nominal flow rate. Furthermore, LES computations have been extended for a wide number of blade events, in order to obtain a representative statistical convergence of the averaged results [11].

All the computations have been completed on a home-made cluster, composed of four parallelized quad-core PCs at 2.67 GHz with 4 GB RAM in each node. The numerical routine adopted for both R-S and S-R configurations started with a steady simulation, followed by a transient unsteady simulation for 20 blade events (2 complete rotor turns) and a final statistically resolved stage for additional 200 blade events (an order of magnitude higher). As a consequence, 6000 time steps have been considered for the database for every simulated condition (7.2 GB of info per case). The CPU time required for each case reached up to 450 hours to obtain a converged statistical description of the unsteady flow patterns.

MATLAB<sup>®</sup> software was used for data processing of the instantaneous velocities and sub-grid turbulent viscosities stored for a planar window in the outlet domain of both configurations. The streamwise extension of these windows corresponded to five chord lengths of the blades, keeping the tangential width to three stator vane pitches (periodicity conditions). A number of home-made codes were developed for interpolation of grids, filtering, relocation in the relative frames and both phase and time averaging. The execution of all these routines also required a significant computational effort.

## 4. Assessment of turbulence transport: metrics and results

Different variables may be used to describe the level and the spatial distribution of the turbulent flow. The most convenient definition is the ensemble-averaging value of the random fluctuations to the square which, in turbomachinery environments, describes the unsteady turbulent field. In other words, it illustrates the transport of the turbulent structures in the unsteady, deterministic flow patterns. Moreover, the unsteady turbulence level can be defined comparing the RMS of that variable with the time-resolved velocity at each blade phase.

To obtain the ensemble-averaged values, a number of blade/vane passages are isolated and classified into a fixed number of phases. Then, averages are performed among the corresponding phases, so that chaotic flow variations may be eliminated, obtaining the unsteady deterministic field. Subsequently, the unsteady flow structures may be filtered out with a further time averaging, obtaining a steady flow pattern. Assuming that there is periodicity between consecutive blades/vanes, the phase- or ensemble-averaged value of a flow variable  $u$  at the phase  $\phi$  (angular position) is obtained as :

$$\tilde{u}(\phi) = \frac{1}{M} \sum_{m=1}^M u_m(t) \quad (1)$$

where,  $M$  is the total number of ensembles and  $u_m(t)$  are the realizations made at times so that  $\phi = \frac{2\pi}{N_B}(m-1) + \omega t$ .  $N_B$  is the number of blades/vanes and  $\omega$  is the rotational speed. The tilde operator ( $\tilde{\cdot}$ ) will be used throughout the text to indicate the ensemble-averaging procedure.

Once the ensemble-averaged values are obtained, the different unsteady scales may be obtained. Turbulence scales are obtained from the subtraction of the ensemble-averaged values to the instantaneous values of the variable, according to  $u'(t) = u(t) - \tilde{u}(\phi)$ . Finally, a second time-averaging operator is introduced to retrieve the mean-time value as follows:

$$\bar{u} = \frac{1}{N} \sum_{n=1}^N \tilde{u}(\phi_n) \quad (2)$$

where  $N$  is the number of time steps between consecutive blade events (it may be also regarded as the temporal discretization of the ensemble-averaged signal). With the mean-time value, the deterministic unsteadiness for every phase is obtained as:  $u''(\phi) = \tilde{u}(\phi) - \bar{u}$ .

Once the different contributions to the total value of the signal have been segregated, the different metrics that describe the flow behaviour may be calculated.

### 4.1. Turbulence and deterministic unsteadiness intensity

The first variable of interest is the turbulence intensity, which represents the turbulent unsteadiness of the flow with respect to the mean values. It is defined as follows:

$$TU(\phi) = \frac{\sqrt{\tilde{u}^2 + \tilde{v}^2}}{\sqrt{u^2 + v^2}} \quad (3)$$

**Figure 3** shows the unsteady evolution of the turbulent structures in the axial fan stage in terms of the turbulence intensity (TU, in percentage). The flow patterns in both R-S and R-S configurations are compared at nominal ( $Q_N$ ) and off-design conditions (70%  $Q_N$ ). Five intermediate instants have been selected to track the time-resolved interaction of rotor and stator

structures ( $t/T_R$  at 0.0, 0.2, 0.4, 0.6 and 0.8, being  $T_R$  the blade-passing time). In the S-R case, the relative frame of reference is represented for the analysis ( $t/T_S$ ). Apart from the evident higher turbulence levels at off-design conditions, the impact of the turbulence of the rotor wakes onto the vanes in the R-S case is much more significant than the slight effect of the vane wakes onto the rotor (S-R). The turbulence level near the leading edge (LE) of the pressure side of the vanes is completely conditioned by the periodic passing of turbulent rotor wakes at 70%  $Q_N$ . In addition, the massive separation of the vanes suction side observed in the R-S is also a consequence of the poor underturning of the meanflow through the rotor passages when operating at low flow rates. Even at nominal conditions, the impact of the rotor wakes on the vanes is evident for the R-S configuration. In the S-R cases, the rotor wakes experience an abrupt thickening as a consequence of the flow rate reduction (from 100 to 70%  $Q_N$ ). At nominal conditions, the rotor wakes do not seem to be significantly conditioned by the incoming stator wakes. On the contrary, rolling-up mechanisms of the larger vortices at 70%  $Q_N$  (see the vortex street on the right column) appear to be chopped by the stator wakes, generating hot spots of turbulence.

Likewise, deterministic fluctuations can be used to define a corresponding level of deterministic unsteadiness (DU). In this case, the deterministic fluctuation is further time-averaged, so a final mean-time footprint of the periodic variations in the stage is retrieved according to:

$$DU = \frac{\sqrt{\overline{u'^2 + v'^2}}}{\sqrt{\overline{u^2 + v^2}}} \quad (4)$$

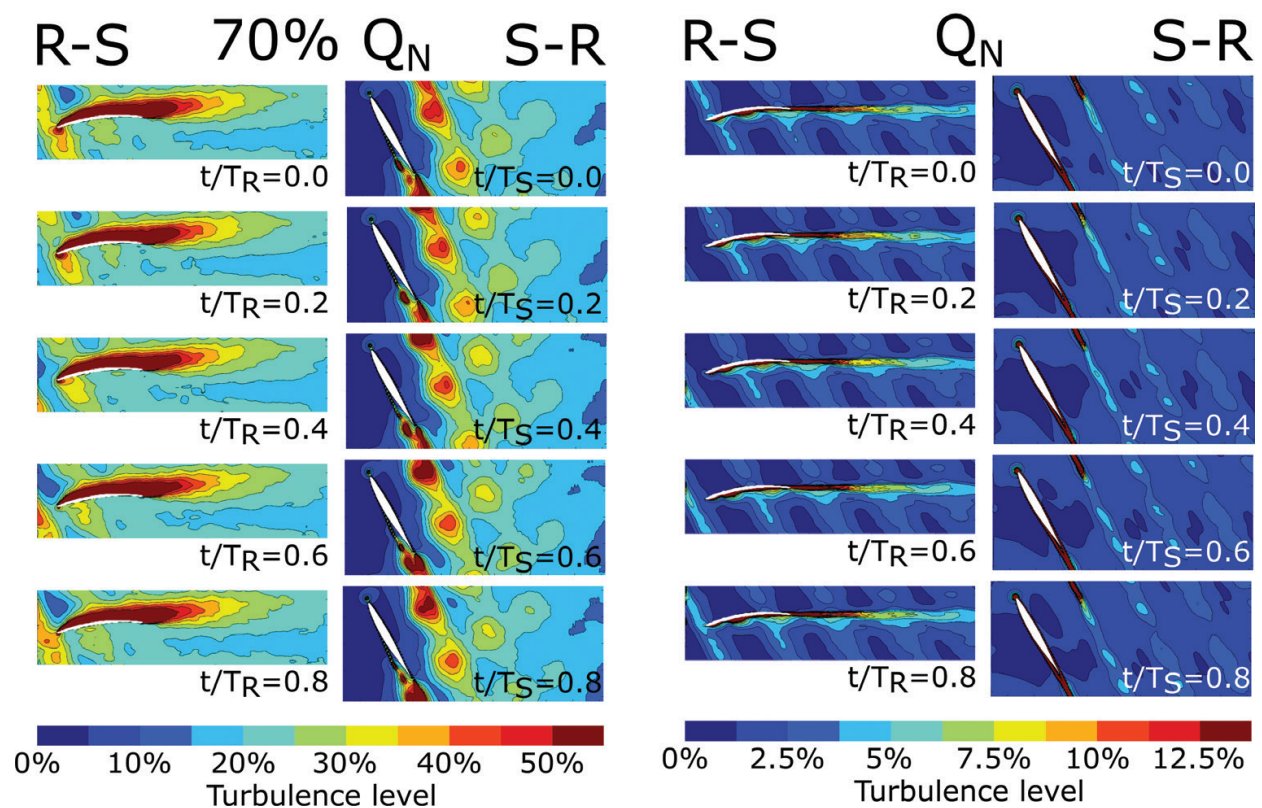


**Figure 3.** Unsteady convection of incoming wakes in stator (absolute in R-S) and rotor (relative in S-R) passages. Nominal flow rate (left) and off-design conditions (right).

**Figure 4** (left) compares, for all the flow rates simulated, those regions in the stage where the intensity of the unsteadiness is prominent. In the case of the R-S configuration, major unsteadiness arises in the axial gap between the rows, where the periodic passing of blades generates a pulsating flow over the vanes and a significant interaction. Maximum levels around 12.5% are observed at off-design conditions, in the inter-row regions (observed as an ‘averaged’ tangential band due to the blade motion) and also on the trailing edge (TE) of the vanes suction side (precisely where turbulence generation appeared to be uncorrelated to deterministic fluctuations). On the contrary, the S-R configuration exhibits large values of unsteadiness at the core of the rotor wakes. This reveals that the intensity of the velocity deficit in the rotor wakes is modulated (up to a significant 15%) by the unmixed stator wakes convected out in the rotor passages. Note that the behaviour of the deterministic unsteadiness is completely opposite in both configurations, though in both cases it is more important at lower flow rates.

In addition, the levels of deterministic fluctuation and turbulence are also compared in **Figure 4**, after computing and representing the mean-time maps of turbulence on the right side. Turbulence levels are always higher than deterministic fluctuations, even at nominal conditions. Approximately, they are 3–5 times higher across the stage, depending on the working conditions. It is noticeable that both deterministic and turbulent sources of unsteadiness present similar distributions in the S-R configuration, while differing notably in the case of the R-S setup. In that case, turbulent mechanisms generated at the blades are not influenced by the periodic passing wakes, thus presenting a negligible wake-blade

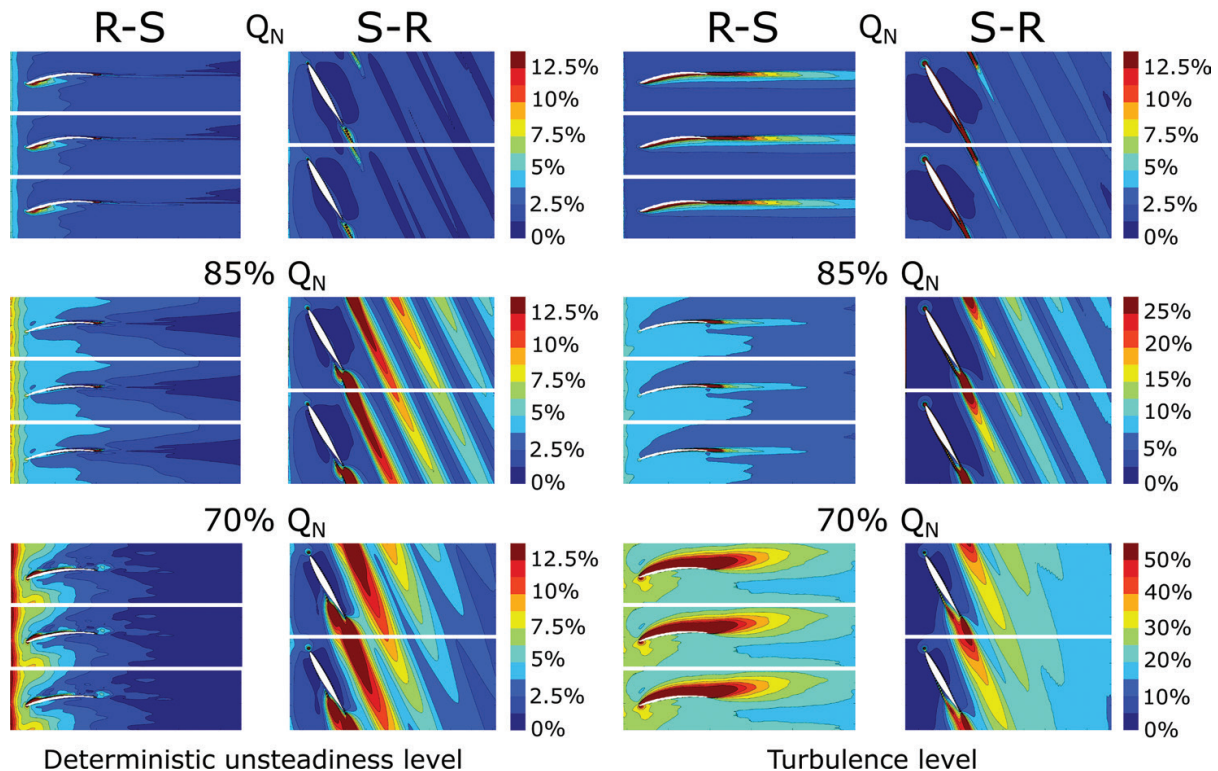


**Figure 4.** Comparison of deterministic unsteadiness (left) and mean time turbulence (right) for R-S and S-R configurations as a function of the flow rate.

interaction. On the other hand, the streamwise convection of the unmixed rotor wakes is clearly chopped by the passing vane wakes in the relative frame, resulting in an evident source of periodic fluctuation.

Previous maps in **Figure 4** can be further pitch-averaged to obtain the streamwise distribution of both deterministic and turbulence levels in the axial fan stage. This third (spatial) operator is essential to assess the impact of these unsteady sources for the modelling of total unsteadiness in the case of through-flow models, because the chordwise distribution of the velocity field obtained is independent of the reference frame (the tangential coordinate is swept out in the averaging). Since the fan stage presents bladed and no-bladed regions, a blockage factor ( $\lambda$ ) [12] has to be introduced to take into account the solidity of the moving blades:

$$\bar{u}^{(\text{thru})} = \frac{1}{\lambda N_\theta} \sum_{\theta=1}^{\lambda N_\theta} \bar{u} \text{ where } \lambda = \frac{N_B(\theta_p - \theta_s)}{2\pi} \quad (5)$$

$N_\theta$  denotes the number of circumferential points per blade passage and  $(\theta_p - \theta_s)$  is the tangential distance between the pressure and suction sides of the blades (function of the axial coordinate).

The pitch-averaged distributions of deterministic and turbulent sources are shown in **Figure 5**. In essence, these plots provide information about those axial positions where the generation of turbulence and deterministic unsteadiness arises. In the case of the R-S configuration (top plots), the deterministic unsteadiness decreases rapidly as it is convected throughout the vane passages, whereas turbulent contributions present a moderate decay. Some local peaks are found near the LE and TE of the vanes due to the influence of stagnant and separated conditions, respectively. The turbulence contours at 70%  $Q_N$  (red line in the right-top plot) reveal the massive separation occurring on the suction side of the vanes (also observed in **Figure 4**, bottom left) that leads to extremely high values of turbulence.

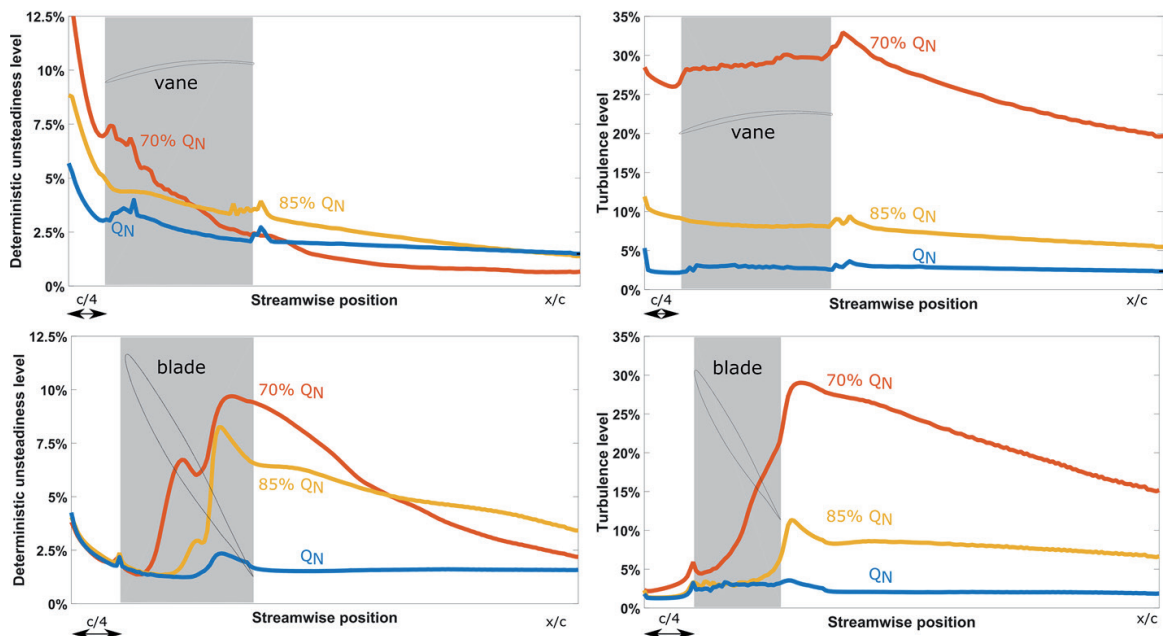


**Figure 5.** Streamwise distributions of pitch-averaged deterministic (left) and turbulent (right) levels for R-S and S-R configurations.

Concerning the S-R configuration, deterministic sources are progressively triggered at earlier chordwise positions as the flow rate is decreased. In addition, at partial flow rates (85 and 70%  $Q_N$ ), a small calm region (local reduction of the unsteadiness) is developed where the turbulence separation is set off (see the corresponding location in the bottom right plot, where the turbulence level is abruptly increased from 10 to 30% at 70%  $Q_N$ ). Once again, this suggests that regions with local turbulence generation are shielded from deterministic fluctuations, whereas further convection of decaying turbulence is more susceptible for intensity fluctuations due to deterministic wake-wake interactions.

#### 4.2. Integral length scales

Another relevant variable is the integral length scale (ILS), which gives an idea of the spatial dimension of the largest eddies of the turbulent structure. Once all the periodic events have been removed from a velocity trace, the integral scale can be estimated from the area under the autocorrelation function—*ACF*—of the signal [13]. This procedure is valid if the average eddy size lies through the correlation of two velocity signals (Taylor's hypothesis of frozen turbulence). Note also that average eddies of a wave number larger than the grid filter of the LES modelling cannot be estimated. Therefore, for this numerical dataset, the ILS has been defined according to:

$$ILS = \bar{u} \int_0^{\infty} ACF(\tau) d\tau \text{ where } ACF(\tau) = \frac{\overline{u'(t)u'(t+\tau)}}{\overline{u'^2}} \quad (6)$$

Again, the overbar denotes the time-averaged value, and  $\tau$  is the time lag that is used to construct the autocorrelation. Due to the inherent randomness of turbulent fluctuations, it is typical to obtain significant scatter in the spatial distribution of the results. For that reason, only an estimated order of magnitude can be given concerning this variable. Moreover, pitchwise averaging has been also introduced to provide a more uniform representation of the results.

As largest vortices evolve across the fan stage, they are stretched and chopped inside the row passages. During convection, their kinematic characteristics are modified, and they can be also reinforced with additional vorticity shedding released from adjacent blades or vanes. In order to provide a comprehensive picture of these vortical dynamics, it is necessary to estimate the size of the largest vortices upstream of the last row in the stage. Besides, it is important to show the streamwise (averaged) evolution of these eddies and their final pitchwise distribution at the fan discharge.

**Table 1** summarizes the characteristic size of the largest eddies within the inter-row region of the stage for every configuration. As expected, typical values around 15–20 mm (in average) are found in the case of the R-S configuration, in concordance with the characteristic thickness of the rotor wake. On the other hand, in the case of the S-R configuration, the value is slightly reduced to 8–10 mm, which also agrees with previous experimental measurements in the stator wakes (around 5 mm [14]). Generally, the ILS values are progressively reduced as the flow becomes turbulent (small scale turbulence in the shear layers of the wakes) with lower flow rates.

Flow rate	Rotor-stator (R-S) (mm)	Stator-Rotor (S-R) (mm)
100% $Q_N$	21.0	9.1
85% $Q_N$	15.3	8.3
70% $Q_N$	14.7	11.3

**Table 1.** Typical values of ILS within the inter-row region as a function of the flow rate.

Following, ILS distributions in the case of the R-S configuration for both streamwise and pitchwise positions at different flow rate conditions are shown in **Figure 6**. The progressive enlargement of the integral scale as the vortices are convected along a streamline (A-A') is noticeable. This feature can be observed in the positive slope shared by the chordwise distributions of all the flow rates studied. ILS levels are significantly increased at the rotor exit (between 25 and 40 mm for all the flow rates) because of the dispersion and mixing-out process suffered by the rotating rotor wakes (the mesh filter is also enlarged, so smaller vortices are transferred to the sub-grid scales and the minimum size of resolved eddies is artificially increased). In the case of 70%  $Q_N$ , the massive vortex shedding (characterized by large recirculation vortices and large-scale instabilities) on the suction sides of the vanes causes a severe increment of the ILS chordwise evolution (bottom-left plot). In the pitchwise distribution (right plot), both 100 and 85%  $Q_N$  present a local value around 10 mm, corresponding to the stator wakes, which is progressively enlarged towards higher values (20–30 mm) in the mid-passage region. For 70%  $Q_N$ , the massive separation is observed as a double-peaked distribution with highest values up to 70 mm. The local minimum is also located in the stator wakes, but with slightly higher values than for the other flow rates, in the range of roughly 20 mm.

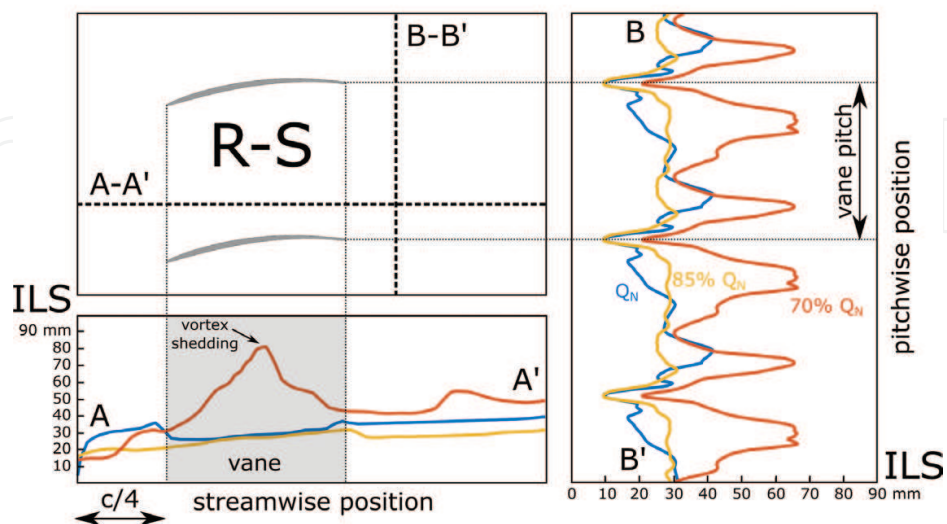


**Figure 6.** Distributions of ILS in the R-S configuration for different flow rates. Streamwise and pitchwise evolutions along lines A-A' (bottom plot) and B-B' (right plot), respectively.

**Figure 7** analyses analogous results for the S-R configuration. The pitchwise distributions reveal again a jet-wake distribution, being clearer for the nominal flow rate. The local minimum is placed at the rotor TE, being similar for all the analysed flow rates, in the range of 4–6 mm. On the other hand, the plot comparing the streamwise evolution according to the flow rates is completely distorted by the excessive vortex shedding coming from the blade separation at 70%  $Q_N$ . This anomaly (ILS up to 70 mm) is rapidly vanished as the streamline reaches the blade TE, where values slightly higher than those found in the inter-row region (see **Table 1**) are recovered. Once again, the advection of large vortices in blade passages tends to increase the outlet values of the ILS. Moreover, a comparison with experimental results in the outlet positions reveals a reasonable agreement, where typical values around 10 mm were estimated with HWA for the nominal flow rate [14].

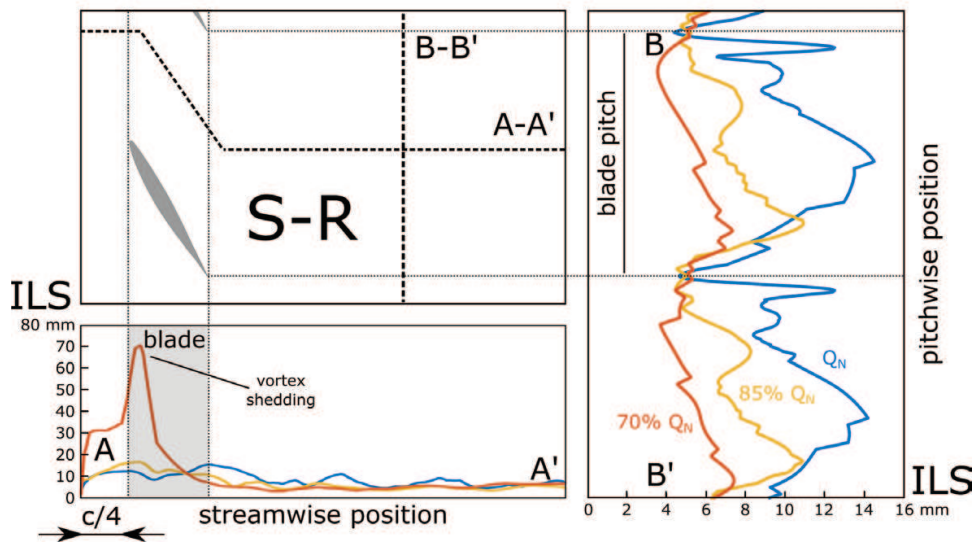


**Figure 7.** Distributions of ILS in the S-R configuration for different flow rates. Streamwise and pitchwise evolutions along lines A-A' (bottom plot) and B-B' (right plot), respectively.

#### 4.3. Turbulent and deterministic stress tensors

Finally, the unsteady kinetic energy may be calculated from the previous segregation of the velocity signals as the content of energy for both deterministic and turbulent contributors. In addition, LES simulations reveal the residual kinetic energy modelled below the grid filter, using the sub-grid turbulent viscosity as its primary contributor.

The turbulent kinetic energy (TKE), defined from the addition of the components of the main diagonal of the Reynolds Stress Tensor at every time step, provides a collection of instantaneous values. For a simpler representation, it is more convenient to time-average the TKE distributions in order to provide a mean-time footprint of the turbulent scales in the flow structures:

$$\tau_{ij}^{(res)} = -\rho \overline{u_i' u_j'} \Rightarrow \overline{K_T} = \frac{1}{2} \tau_{ii}^{(res)} = \frac{1}{2} \rho (\overline{u'^2} + \overline{v'^2}) \quad (7)$$

It is important to recall that this formulation gives only the resolved part of the whole turbulent energy budget. A complete estimation of the TKE requires the summation of the additional

sub-grid TKE over the resolved part in the case of LES computations. However, the sub-grid component is quite marginal when a rough estimation of the resolved energy is around an 80%. In this case, it is acceptable to consider the resolved part as the major contributor, obviating the sub-grid scales. In Section 4.4, this assumption will be contrasted from the comparison of both resolved and sub-grid components.

In a similar fashion, the time-averaged value of the deterministic fluctuations leads to the definition of the deterministic stress tensor, which formulation resembles the turbulent one but in the case of the unsteady (periodic) fluctuations coming from the rotating blades. Mathematically speaking, this may be expressed as:

$$\tau_{ij}^{(det)} = -\rho \overline{u_i'' u_j''} \Rightarrow \overline{K_D} = \frac{1}{2} \tau_{ii}^{(det)} = \frac{1}{2} \rho (\overline{u''^2} + \overline{v''^2}) \quad (8)$$

where the deterministic kinetic energy (DKE) is computed from the addition of the components of the main diagonal of the tensor.

**Figure 8** compares the mean-time maps of TKE and DKE for S-R and R-S configurations for both 100 and 70%  $Q_N$  working conditions. The values have been made dimensionless with the squared blade velocity for all the cases. Two significant features can be highlighted: firstly, concerning the configuration, it is evident that TKE is notably higher in the case of the R-S configuration with respect to the S-R case, independently of the operating conditions. Conversely, DKE is higher in the S-R arrangement, especially for the off-design flow rate. The massive separation in the vanes suction side for the R-S case and the flow detachment in the blades for the S-R case, both at 70%  $Q_N$  are the responsible mechanisms for this inverted trend. Secondly, regarding the flow rate, it is evident the reinforcement of the different mechanisms for reduced flow conditions. In addition, in the R-S configuration, the distributions of TKE and DKE present local maxima that differ significantly from 100 to 70%  $Q_N$ . This characteristic is not replicated in the S-R case.

The complete Reynolds Stress Tensor is shown in **Figure 9**. As expected, in the R-S configuration, the pure axial components are clearly larger than the tangential components due to the chordwise alignment of the bulk flow. On the contrary, the relative flow in the S-R arrangement, with a blade outlet angle of 60°, makes both components equally important. Also, the

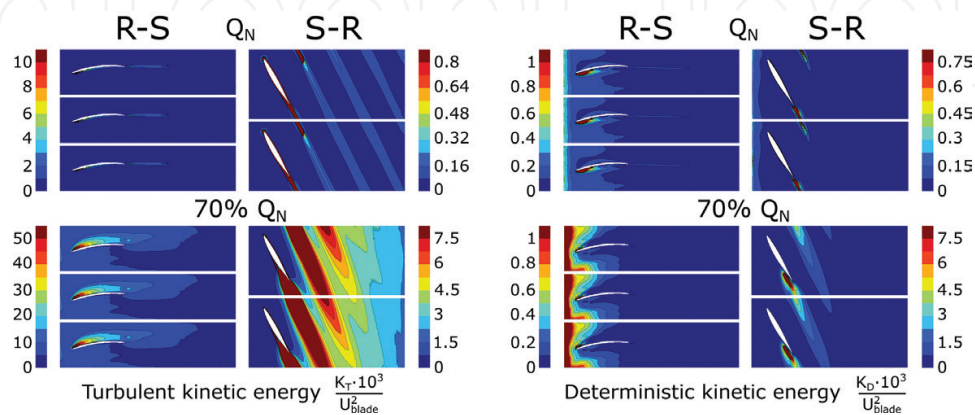


**Figure 8.** Time-averaged maps of Turbulent (left) and Deterministic (right) Kinetic Energy for R-S and S-R configurations. Comparison of nominal (top) and off-design (bottom) conditions.

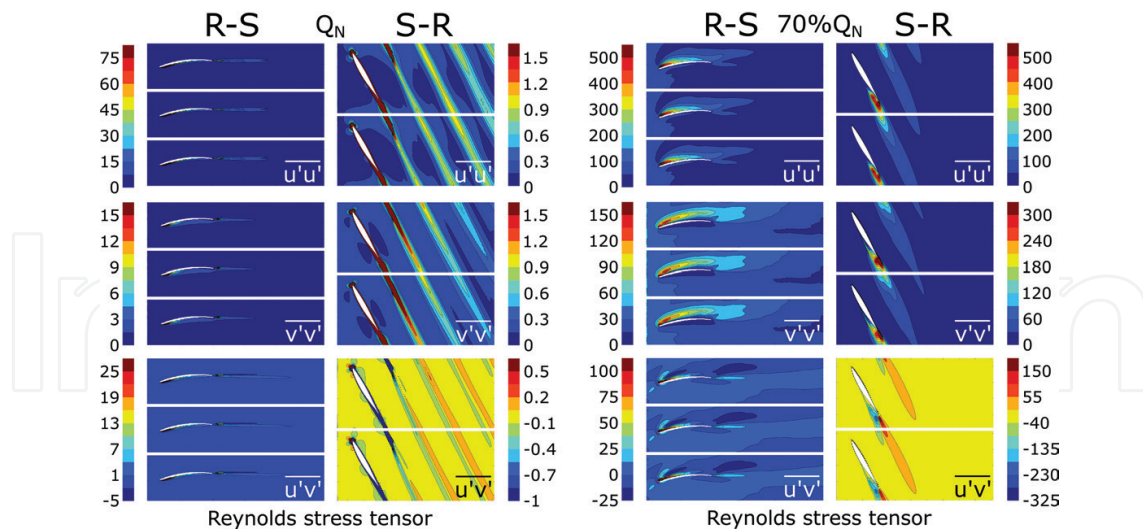


**Figure 9.** Components of the Reynolds Stress Tensor for both configurations. Comparison of nominal (left) and off-design (right) conditions.

crossed-component reveals the appearance of shear stress layers with opposite signs, which is a characteristic feature of wake or jet flows. At 70%  $Q_N$ , the turbulent crossed-component of the tensor shows significantly high levels, suggesting an appreciable correlation between axial and tangential randomness. This can be interpreted as an enhanced turbulent mixing in the rotor wakes.

This section is concluded presenting the deterministic stress tensor in **Figure 10**. The identification of the deterministic tensor is an essential tool to model with accuracy the effects of unsteadiness in the design of multistage turbomachinery using 1D through flow codes or conventional steady mixing-plane approaches [15, 16]. The proposal of transport models

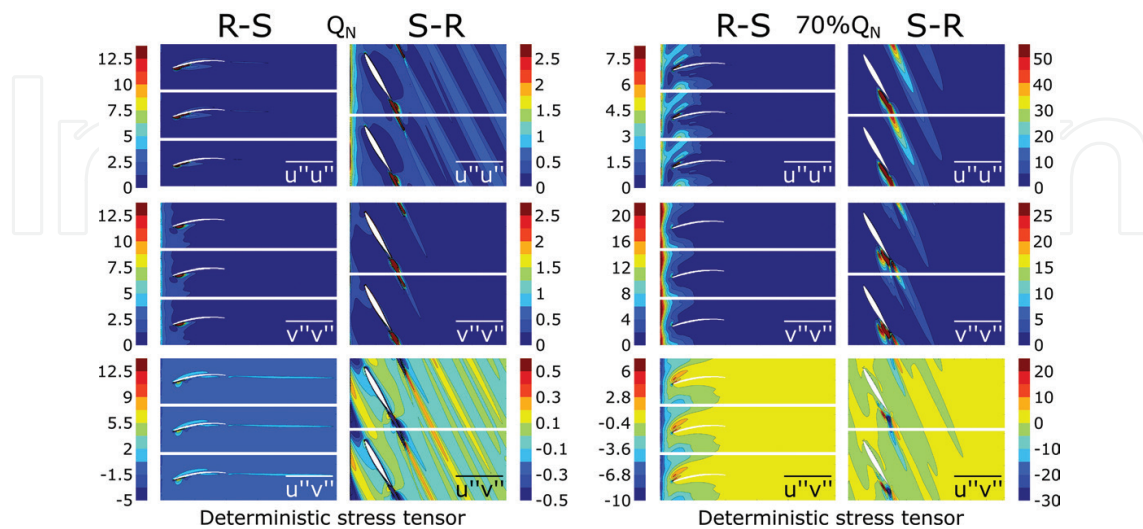


**Figure 10.** Components of the deterministic stress tensor for both configurations. Comparison of nominal (left) and off-design (right) conditions.

for deterministic stresses must be necessarily based on empirical correlations and, also, in a wide range of numerical experiments to validate the approaches [17]. In the S-R arrangement, modelling efforts must be driven towards the rotor wakes, where all the components are concentrated near the TE of the blades, being more intense at low flow rates. In the case of R-S configuration, the tensor components present a more complex behaviour, with local maxima near the LE of the vanes for all the components of the tensor at 100%  $Q_N$ , whereas the inter-row regions, with the predominance of the tangential correlation, are the major sources of unsteadiness at 70%  $Q_N$ .

#### 4.4. Other metrics: degree of anisotropy and sub-grid TKE

Due to the importance of both axial and tangential components in the definition of the Stress Tensors, a final effort has been made to identify their relative importance. For that purpose, an additional indicator, the degree of anisotropy, has been defined to quantify the departures from isotropy of the flow structures associated to both turbulent and deterministic unsteadiness. For this investigation, the degree of anisotropy has been evaluated by comparing time-averaged values of turbulent and unsteadiness according to:

$$DA_T = \frac{\sqrt{u'^2} - \sqrt{v'^2}}{\sqrt{u'^2} + \sqrt{v'^2}} \quad \text{and} \quad DA_D = \frac{\sqrt{u''^2} - \sqrt{v''^2}}{\sqrt{u''^2} + \sqrt{v''^2}} \quad (9)$$

With this definition (adapted from [18]), the degree of anisotropy is always comprised between  $-1$  and  $1$ . When this parameter is close to zero, the flow structure presents a clear isotropic characteristic. On the contrary, higher levels close to  $1$  indicate anisotropic patterns, being the axial component prominent, while lower values around  $-1$  indicate also anisotropy but with the tangential component as the major contributor.

Turbulence has been found to be mainly isotropic for all the analysed cases. **Figure 11** (left) reveals low levels of anisotropy in the stator passages, mainly encapsulated around the vane surfaces. Only at nominal conditions, the stator wake is clearly anisotropic with the axial fluctuation being dominant. In the case of the S-R, the pattern is similar, with only a slightly higher anisotropy in the rotor wakes. The tangential components appear more important due to the background deviation of the flow. At 70%  $Q_N$  the tangential anisotropy is also limited to the blade surfaces.

Alternatively, the deterministic flow exhibits a clear anisotropy behaviour for both configurations (**Figure 11**, right). Moreover, the anisotropy is more complex and intense in the case of low flow rates. For both R-S and S-R arrangements, the axial anisotropic is evident at nominal operating conditions. In the R-S, it is associated to the stator wakes, while in the S-R this feature is linked to the inner passages. However, at 70%  $Q_N$  large regions of tangential anisotropy arise as a consequence of the enhanced mixing-out of the wakes (higher fluctuations). Even, for the R-S case, a hot spot is clearly established one chord downstream of the vanes; while for the S-R case a tangential band is formed instead.

In order to validate the previous assumptions, it is necessary to study the levels of sub-grid turbulent kinetic energy. Higher percentages of resolved TKE with respect to the total turbulent budget (at least, around an 80%) are required to make LES simulations representative of the turbulent motion [19]. For this dataset, the sub-grid TKE has been obtained from the post-processing

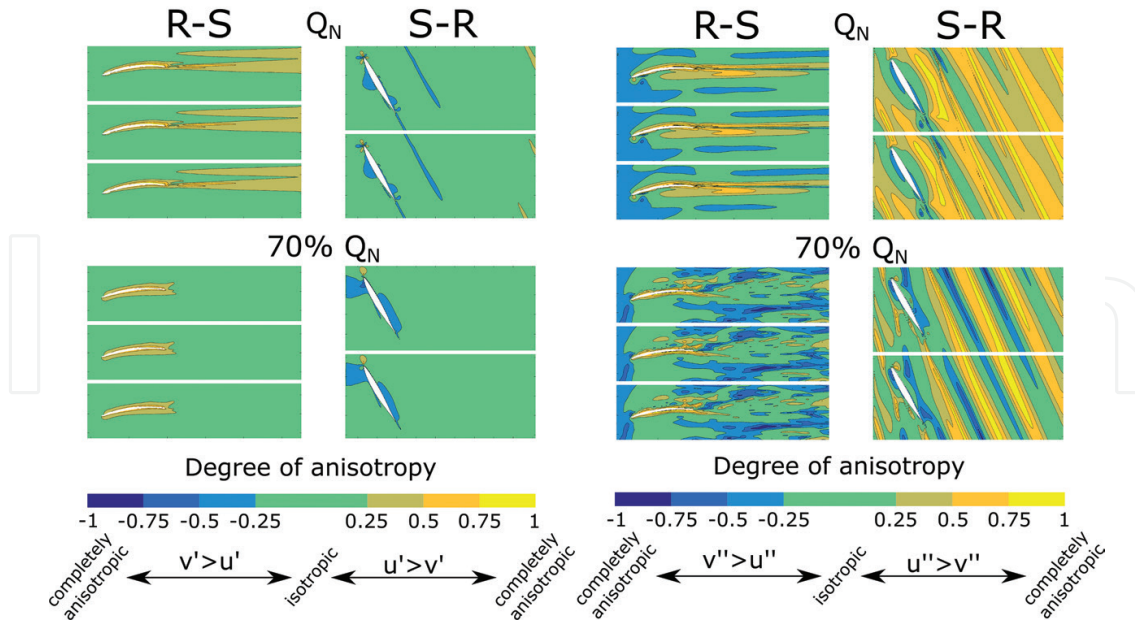


**Figure 11.** Degree of anisotropy for turbulent components (left) and deterministic unsteadiness (right) in both setups. Comparison of nominal (top) and off-design (bottom) conditions.

of the sub-grid turbulent viscosity maps given by the model equations. After some dimensional considerations [20], the sub-grid TKE can be calculated from:

$$K_{sgs} \simeq \mu_T^2 / \rho^2 (C_s \Delta)^2 \quad (10)$$

where  $\Delta = (\Delta x \Delta y \Delta z)^{1/3}$  stands for the averaged size of a computational cell and  $C_s$  is the Smagorinsky constant. This constant has been set to 0.1, as this value has been found to yield the best results for a wide range of flows.

**Figure 12** shows instantaneous maps of the sub-grid turbulent viscosity ratio,  $\mu_T/\mu$ , for both R-S (top) and S-R (bottom) configurations for different flow rate conditions. These maps reveal the regions where sub-grid turbulence levels arise as consequence of an important turbulent generation at small-scales. As well, they highlight how the global level of disorder is progressively increased as the flow rate decreases. In the R-S case, there is high turbulence intensity in the stator passages, derived from the high levels of turbulence production in the rotor wakes, hence further convected downstream. In the relative frame of reference for the S-R configuration, the generation of turbulence in the rotor wakes is so large and evident that the stator turbulence is completely masked. Consequently, this second configuration is less turbulent and, despite of being a worse design in terms of noise generation, it is a moderate contributor for interaction with less viscous dissipation than the former case.

With these instantaneous maps, applying the previous equation for the estimation of the sub-grid TKE, it is possible to compare the sub-grid TKE values with the post-processed, time-resolved TKE and define the percentage of TKE that it is really resolved by the LES modelling. **Figure 13** summarizes, for both configurations, the typical levels of resolved TKE. It is determined that background levels around 90% provide an accurate framework for the present analysis of the turbulent transport in axial fan stages. These levels are sufficiently high to consider

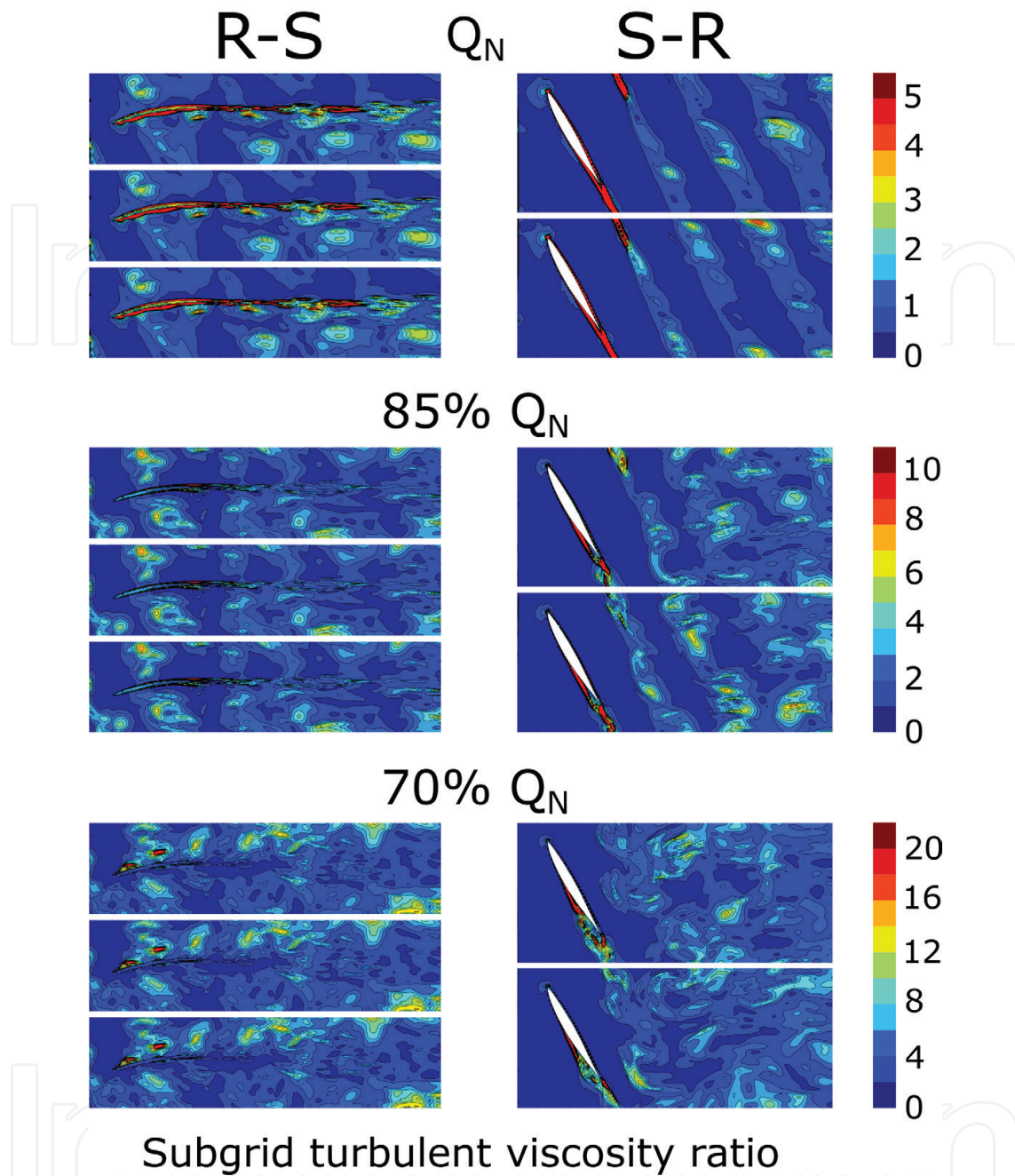


**Figure 12.** Generation of sub-grid turbulent viscosity at different flow rate conditions. Comparison of R-S (top) and S-R (bottom) configurations.

the present numerical database as a highly resolved LES simulation. Lower levels of resolved TKE are found in the viscous regions of the flow, especially associated to those regions of turbulence generation: on the vicinity of blade and vane surfaces and also in turbulent spots where superimposed viscous structures collide to reinforce vorticity sources (i.e. wake-wake interactions). Regarding the impact of the flow rate, it is evident that nominal conditions require a higher level of modelled turbulence, in both stator and rotor wakes, due to lower size of the vortices shed at high Reynolds numbers [21]. As the flow rate is progressively reduced, the

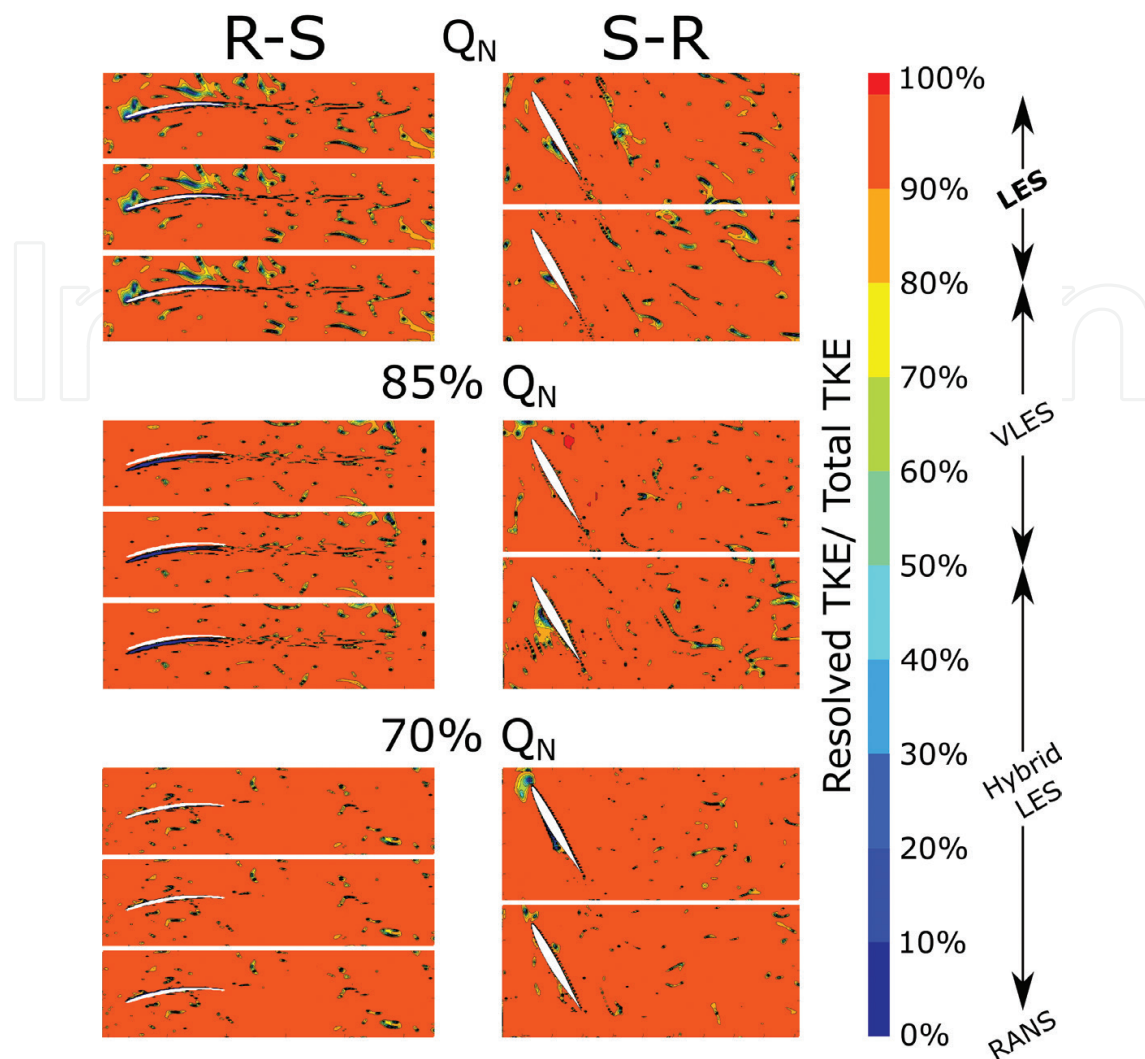


**Figure 13.** Percentage of resolved kinetic energy in the LES computations. Comparison of R-S and S-R configurations at nominal (top) and off-design (bottom) conditions.

larger size of the detached vortices reduces the percentage of modelled energy in the LES computations accordingly.

## 5. Conclusion

A comprehensive overview of unsteady deterministic scales, compared to turbulent ones, when both basic rotor-stator and stator-rotor configurations are analysed in the case of low-speed axial fans is presented. A 3D numerical simulation using LES algorithms has been employed to obtain the unsteady flow patterns within the single axial stages as a function of the operating conditions. Afterwards, an intensive post-processing has been performed to disclose deterministic maps as well as the turbulent structure of the flow, revealing its unsteady transport and the typical size of integral scales and their turbulence levels.

In summary, it has been shown that in the inter-row region of the R-S configuration, the periodic passing of rotor wakes is the main interaction mechanism, as it may be observed in the deterministic unsteadiness of the flow. On the other hand, for the S-R configuration, the major interaction mechanisms are viscous and are associated to wake-wake interactions between the unmixed lattice of rotor wakes and the stator shear layers.

This methodology may be applied to assess the unsteady effects on the dynamic performance and overall efficiency of prospective as well as commercial fan designs. Detrimental frequencies may be predicted, and the study of turbulent effects may lead to improvements in design to produce lower noise levels, as well as to achieve a better flow guidance that leads to less energy losses. Finally, the segregation and study of the deterministic part of the fluctuations leads to a better knowledge of the fan working principles. This represents a significant advantage for fan designers, as the deterministic part of the flow may be used to maximise energy exchange.

## Author details

Jesús Manuel Fernández Oro\*, Andrés Meana Fernández and Bruno Pereiras García

\*Address all correspondence to: [jesusfo@uniovi.es](mailto:jesusfo@uniovi.es)

Fluid Mechanics Area, Department of Energy, University of Oviedo, Asturias, Spain

## References

- [1] Menter, F.R., Schütze, J., Kurbatskii, K.A., Gritskevich, M., Garbaruk, A., (2011), "Scale-Resolving Simulation Techniques in Industrial CFD", Proceedings of the 6th AIAA Theoretical Fluid Mechanics Conference, AIAA2011-3474, June 27-30, Hawaii (USA).
- [2] Tucker, P.G., (2013), "Trends in Turbomachinery Turbulence Treatments", Progress in Aerospace Sciences, 63, pp. 1-32.
- [3] Shur, M.L., Spalart, P.R., Strelets, M.K. and Travin, A.K., (2008), "A Hybrid RANS-LES Approach with Delayed-DES and Wall-Modeled LES Capabilities", International Journal of Heat and Fluid Flow, 29, pp. 1638-1649.
- [4] Adamczyk, J.J., (2000), "Aerodynamic Analysis of Multistage Turbomachinery Flow in Support of Aerodynamic Design", ASME Journal of Turbomachinery, 122, pp. 189-217.
- [5] Goto, A., (1992), "Three-Dimensional Flow and Mixing in an Axial Flow Compressor with Different Rotor Tip Clearances", ASME Journal of Turbomachinery, 112, pp. 675-685.
- [6] Lakshminarayana, B., (1981), "Techniques for Aerodynamic and Turbulence Measurements in Turbomachinery Rotors", ASME Journal of Engineering and Power, 103, pp. 374-392.
- [7] Camp, T.R., Shin, H.-W., (1995), "Turbulence Intensity and Length Scale Measurements in Multistage Compressors", ASME Journal of Turbomachinery, 117, pp. 38-46.

- [8] Fernández Oro, J.M., Argüelles Díaz, K.M., Blanco Marigorta, E., 2009, "Non-Deterministic Kinetic Energy within the Rotor Wakes and Boundary Layers of Low-Speed Axial Fans: Frequency-Based Decomposition of Unforced Unsteadiness and Turbulence", *Journal of Turbulence*, 10, N28.
- [9] Davidson, L., Dahlström, S., (2005), "Hybrid LES-RANS: An Approach to Make LES Applicable at High Reynolds Numbers", *International Journal of Computational Fluid Dynamics*, 19 (6), pp. 415-427.
- [10] Galdo Vega, M., Rodríguez Lastra, M., Argüelles Díaz, K.M., Fernández Oro, J.M., (2012), "Application of Deterministic Correlations in the Analysis of Rotor-Stator Interactions in Axial Flow Fans". Proceedings of the ASME 2012 Fluids Engineering Summer Meeting, FEDSM2012-72450, July 8-12, Puerto Rico (USA).
- [11] Fernández Oro, J.M., Argüelles Díaz, K.M., Rodríguez Lastra, M., Galdo Vega, M., Pereiras García, B., (2014), "Converged Statistics for Time-Resolved Measurements in Low-Speed Axial Fans using High-Frequency Response Probes", *Experimental Thermal and Fluid Science*, 54, pp. 71-84.
- [12] Persico, G., Rebay, S., (2012), "A Penalty Formulation for the Throughflow Modeling of Turbomachinery". *Computers and Fluids*, 60, pp. 86-98.
- [13] Tropea, C., Yarin, A.L., Foss, J.F., (eds.), *Handbook of Experimental Fluid Mechanics*. Ch. 10. "Measurement of Turbulent Flows", pp. 745-855, Springer, New York, (2008).
- [14] Fernández Oro, J.M., Argüelles Díaz, K.M., Santolaria Morros, C., Blanco Marigorta, E., (2007), "On the Structure of Turbulence in a Low-Speed Axial Fan with Inlet Guide Vanes", *Experimental Thermal and Fluid Science*, 32, pp. 316-331.
- [15] Adamczyk, J.J., (1996), "Modelling the Effect of Unsteady Flows on the Time Average Flow Field of a Bladerow embedded in an Axial Flow Multistage Turbomachine", VKI Lecture Series, on Unsteady Flows in Turbomachines, 1996-05, Von Karman Institute for Fluid Mechanics, Brussels (Belgium).
- [16] Meneveau, C., Katz, J., (2002), "A Deterministic Stress Model for Rotor-Stator Interactions in Simulations of Passage-Averaged Flow", *ASME Journal of Fluids Engineering*, 124, pp. 550-554.
- [17] Stollenwerk, S., Kügeler, E., (2013), "Deterministic Stress Modeling for Multistage Compressor Flowfields", Proceedings of the ASME Turbo Expo 2013, GT2013-84860, June 3-7, San Antonio (USA).
- [18] Porreca, L., Hollestein, M., Kalfas, A.I., Abhari, R.S., (2005) "Turbulence Measurements and Analysis in a Multistage Axial Turbine", Proceedings of the 17th International Symposium on Air Breathing Engines, ISABE2005-1032, September 4-9, Munich (Germany).
- [19] Pope, S.B., *Turbulent Flows*, Cambridge University Press, New York, (2000).
- [20] Bailly, C., Comte-Bellot, G., *Turbulence*, Springer, Switzerland, (2015).
- [21] Tennekes, H., Lumley, J.L., *A First Course in Turbulence*, MIT Press, Massachusetts, (1972).